ADVANCED FUNCTIONAL MATERIALS
www.afm-journal.de

Hygro-Dynamic and Conductive Actuator That Restructures and Heals by Water

Qing Chen, Tina Künniger, Qun Song, Kai Zhang, Andrei Chumakov, Yusuf Bulut, Constantin Harder, Peter Müller-Buschbaum, Stephan V. Roth,* and Artur Braun**

The prospects of endowing stimuli-responsive materials with various life-like behaviors are promoting the development of intelligent robotic and electronic devices. However, it is challenging to incorporate stimuli-responsive actuating and healing capabilities into one single material system. Herein, the design and assembly of humidity-responsive thin films composed of poly(3,4-ethylenedioxythiophene):polystyrene sulfonate (PEDOT:PSS) and sodium carboxymethyl cellulose (NaCMC) forming a conducting polymer composite through a physically cross-linked and hydrogen-bonded supramolecular network are described. Owing to its enhanced dynamics of hydrogen bonding at an elevated humidity, the PEDOT:PSS/NaCMC thin film exhibits a rapid humidity-responsive actuating performance in an environment with humidity gradient, as well as a repairing function of the structural, mechanical, electrical, and actuating properties after being damaged through a humidifying-drying cycle. Based on a combined analytical approach, a structural model is proposed for the rearrangement of the thin film when being exposed to stepwise humidity levels at multi-length scales. Due to the structural rearrangement powered by humidity variations, the film exhibits tunable actuating and healing performance, which makes it a promising candidate material for applications in intelligent soft robotics such as artificial muscles.

1. Introduction

For many living organisms, the ability to self-adaptate and self-healing with the aid of environmental stimuli is necessary for survival.[1] By extending the vital functionalities of living organisms to the field of soft robotics, artificial materials responding to various stimuli such as light, humidity, or pH have been developed.[2] The structural rearrangement of artificial materials powered by external energy sources offers great potential for the development of sustainable robots,[3] wearable sensors,[4] human-machine interfaces, and soft actuators.[5] These structurally rearrangeable materials can reversibly change their geometrical shape,[6] volume,[7] or the underlying physio-chemical properties in response to external stimuli.[8] Although the inherent flexibility of structurally rearrangeable materials is the key to their adaptability, it also renders them prone to damage. For example, most soft actuators fail to withstand scratch or fracture due to the lack of a healing capability, which leads to deteriorated performance.[9] Thus, there is an increasing demand for developing stimuli-responsive actuators with healing abilities, to prepare such dynamic systems for adaptive and durable applications.[10] However, to date, achieving stimuli-responsiveness without compromising the healing ability within one single material remains challenging.

The basic origin of such challenges is the critical differences, which exist between the structural requirements of

Q. Chen, A. Braun
Laboratory for High Performance Ceramics, Empa
Swiss Federal Laboratories for Materials Science and Technology
Überlandstrasse 129, Dübendorf 8600, Switzerland
E-mail: chenqink1990@gmail.com; artur.braun@alumni.ethz.ch
T. Künniger
Cellulose and Wood Materials, Empa
Swiss Federal Laboratories for Materials Science and Technology
Überlandstrasse 129, Dübendorf 8600, Switzerland
The ORCID identification number(s) for the author(s) of this article can be found under https://doi.org/10.1002/adfm.202402924

DOI: 10.1002/adfm.202402924

Q. Song, K. Zhang
Sustainable Materials and Chemistry
Department of Wood Technology and Wood-based Composites
University of Göttingen
Büsgenweg 4, 37077 Göttingen, Germany
A. Chumakov, Y. Bulut, C. Harder, S. V. Roth
Deutsches Elektronen-Synchrotron DESY
Notkestr. 85, 22607 Hamburg, Germany
E-mail: svroth@kth.se
Y. Bulut, C. Harder, P. Müller-Buschbaum
Department of Physics
Chair for Functional Materials
TUM School of Natural Sciences
Technical University of Munich
James-Franck-Str. 1, 85748 Garching, Germany
S. V. Roth
Department of Fiber and Polymer Technology
KTH Royal Institute of Technology
Teknikringen 56-58, Stockholm 10044, Sweden

stimuli-responsive actuating materials and healable materials. Incorporating dynamic covalent bonds or dynamic non-covalent bonds into stimuli-responsive polymers is a classical strategy to introduce healing ability to stimuli-responsive actuators.[11] However, most of the dynamic bonds require a catalyst or control of environmental conditions to enhance or diminish the reversibility of the bond,[12] which needs to be fine-tuned to balance healing ability/mechanical strength and actuation deformation to adapt the material toward unique applications. Vice versa, stimuli-responsive materials based on strong covalent bonds usually exhibit a powerful actuation performance but suffer from low chain mobility of the polymers, which is likely to reduce the healing efficiency.[13] Moreover, to avoid any unintentional structural rearrangement in either the *non-actuated* or the *non-injured* state, the structural rearrangement of the material needs to be kept deactivated in the static state and activated only by special stimuli when needed.

In this work, we design a structurally-rearrangeable material as a thin film, based on conducting polymer composites with humidity-induced actuating and healing performance. Herein, we refer to "structural rearrangement" to stimuli-induced structural changes at all length scales in addition to the bending deformation of the actuator at the macroscale. The structural rearrangements have been monitored by four in situ analytical techniques targeting different spatial dimensions, in which 1) the destruction/reconstruction of the chemical bonds is detected by Fourier-transform infrared spectroscopy (FTIR), 2) the water absorption/desorption ability is detected by dynamic vapor sorption (DVS), 3) the visco-elastic properties are probed by dynamical mechanical analysis (DMA), and 4) the structural changes at the nano- to sub-microscale are quantified by ultra-small-angle X-ray scattering (USAXS) equipped with humidity control, respectively. These in situ analytical approaches allow us to combine the external energy inputs with the structural evolution of the material, and propose a model, which describes the humidity-induced structural rearrangement of the thin film. With this model, we discuss the regulation of the mechanical and electrical properties of the polymer thin film with respect to relative humidity, in which the restructuring of the thin film can contribute to a healing capability. Moreover, based on this thin film, a humidity-responsive actuator is fabricated to demonstrate its load-lifting performance. This work not only aims to address the conflict between achieving stimuli-responsive actuation and healing capabilities in a single material, but also to test the availability of a novel platform for constructing structurally rearrangeable materials for various actuating and sensing applications.

2. Results and Discussion

2.1. Design and Fabrication of the Humidity-Responsive Thin Film

Stimuli-responsive polymers have been identified recently as promising candidates for synthesizing healable actuators,[14] where the healing function can be triggered by the combined action of the dynamic responses of the stimuli-responsive polymer and the external energy inputs,[15] such as moisture,[16] heat,[17] and pressure.[18] Therefore, the modular assembly,[19] repair,[20] and restructuring of the actuators based on the stimuli-responsive polymer can be achieved under certain stimuli.[21] Following this route, we design a humidity-responsive thin film by embedding a rigid humidity-responsive polymer into a soft polymer matrix, in which the rigid polymer forces the soft matrix to reversibly absorb and desorb moisture, leading to a differential degree of the swelling-induced structural changes in the composite thin film.

The polymer blend poly(3,4-ethylenedioxythiophene):polystyrene sulfonate (PEDOT:PSS) is used as the rigid stimuli-responsive polymer due to its excellent restructuring,[22] actuating,[23] repairing,[24] and healing performance[25] in response to humidity variations. Sodium carboxymethyl cellulose (NaCMC) is chosen to provide a soft phase among the PEDOT:PSS scaffold to obtain favorable mechanical properties. Besides, due to the multiple H-bonding sites, thin films composed of NaCMC feature both, hygroscopic swelling and healing abilities.[26] NaCMC has a stronger hygroscopic property than pure CMC due to the negative ions of -COO^- groups in addition to the -COOH groups. The supramolecular network forms via hydrogen-bonding (H-bonds) and electrostatic interactions between NaCMC and PEDOT:PSS in the PEDOT:PSS/NaCMC composite thin film, which is denoted as "PPC thin film" in the following. Hydrogen bonding may form not only between the oxygen atoms of the -$SO3^-$ groups of PSS^- and the hydrogen atoms of the -COOH groups of the side chains of NaCMC, but also with the hydrogen atoms of the -OH groups of the cellulose backbone of NaCMC.[27] The PPC thin films are prepared via drop-casting of the mixture of PEDOT:PSS and NaCMC dispersions (**Figure 1a**; Figure S1, Supporting Information). Moreover, the counter ion interactions among Na^+CMC and PSS^- can increase the connectivity of the polymer matrix,[28] thus facilitating the transport of moisture and charge carriers. The hydrogen-bonded network between the scaffold and the matrix of the composite is crucial to the structural rearrangement of the thin film under humidity variations indicated in Figure 1b.[29]

2.2. Humidity-Responsiveness at the Molecular, Nano- and Micro-Scales

For humidity-responsive actuators, which perform reversible bending deformation, requirements for designing the topology of the material should be considered: i) a dense network of H-bonds is necessary to allow for effective interaction with water (absorption), and ii) sufficient effective porosity is desirable for the mass transfer of water (desorption). To test the validity of our design, Fourier-transform infrared (FTIR) spectra are recorded during the soaking/drying treatment of a wetted PPC thin film with the hydrogen/deuterium (H/D) exchange method (T = 25 °C, RH = 30%). As evidenced by Figure 1c, the weakening transmission at 3344 cm^{-1} (—OH stretching mode) is accompanied by the enhancing transmission at 2489 cm^{-1} (—OD stretching mode) immediately after D_2O soaking. Simultaneously, the position of the —OH stretching vibration is blue-shifted to 3370 cm^{-1}. As the drying time increases, the intensity of the signature of the —OD stretching at 2489 cm^{-1} decreases, and the —OH signal is gradually restored and red-shifted to 3344 cm^{-1} after 10 min. This redistribution of spectral weights is in accordance with literature that reports the continuous H/D exchange between D_2O

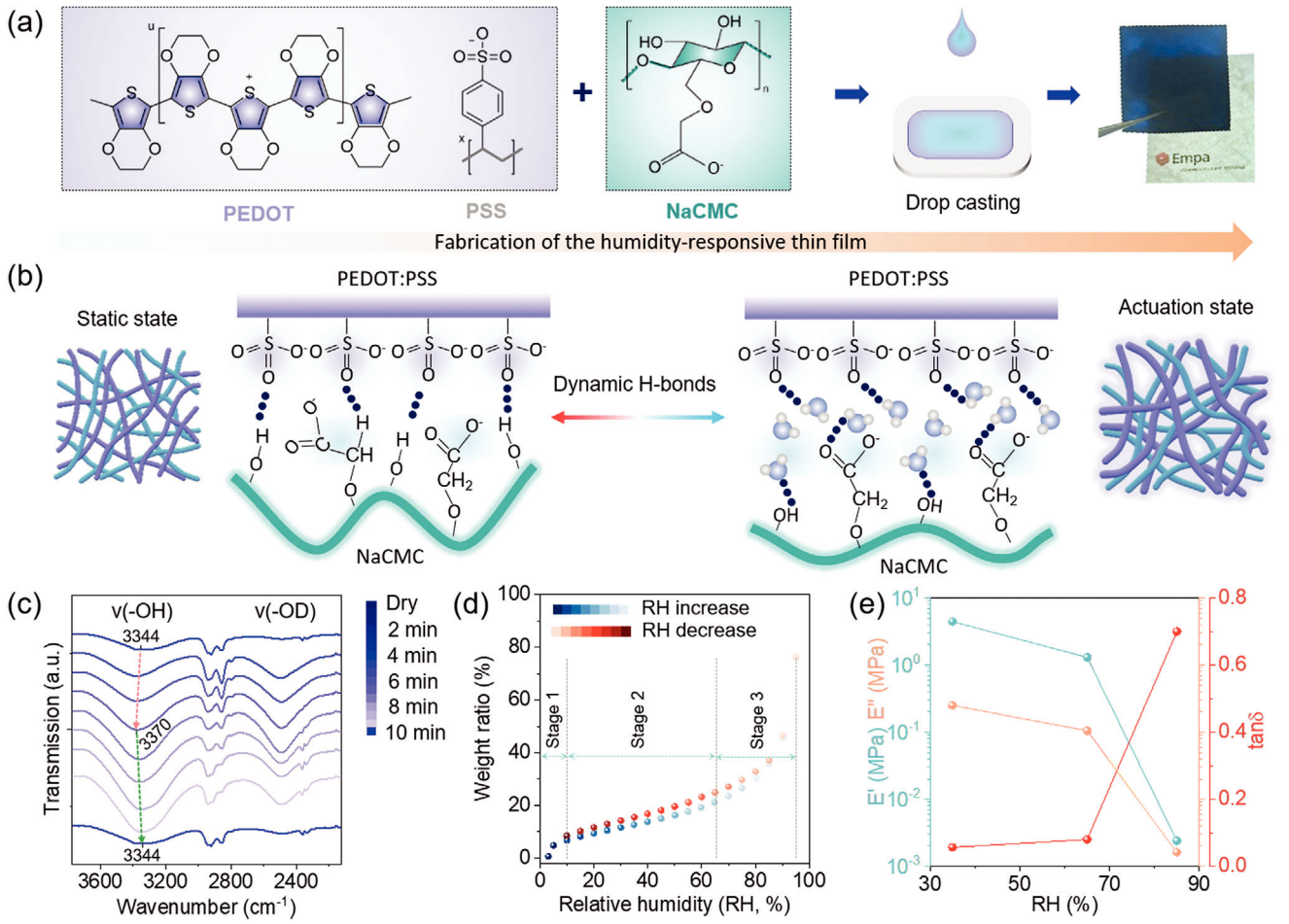

Figure 1. Design and fabrication of the humidity-responsive PEDOT:PSS/NaCMC thin film. a) Schematic of the fabrication process of the humidity-responsive thin film incorporating PEDOT:PSS and NaCMC. This is called PPC thin film in the rest of the manuscript. b) Schematic diagram of the hydrogen bonding and electrostatic interactions among the polymer chains of PEDOT:PSS and NaCMC. When being exposed to moisture: c) Demonstration of the reversible hydrogen bonding (H-bonds) in the PPC film (sample size: 5 mm × 5 mm) by FTIR with hydrogen/deuterium (H/D) water exchange. The orange and green dashed arrows guide to the eye the blue-shifting and red-shifting of the characteristic peak of the —OH groups through the diffusion of D_2O into the film, and the H/D exchange between the air and the film, respectively. d) DVS analysis of the PPC thin films (sample weight: 10 mg), which illustrates the water-absorbing ability of the film during a stepwise hydration/dehydration cycle. The color bar represents the humidity condition at which the value of the water-absorption ratio is recorded. The light green arrows illustrate the three stages of water absorption. For both FTIR and DVS measurement, three samples are tested, from which the data of one sample is used for analysis. e) DMA of the PPC films (sample size: 60 mm × 8 mm) with humidity control, where 35%, 65%, and 85% are chosen as the representative RH levels. Three samples are tested at each RH level to obtain an average value.

in the film and H_2O in the air.[30] The lamellar architecture observed in the scanning electron microscopy (SEM) micrographs of the PPC thin film, which is absent in pure PEDOT:PSS and NaCMC thin film fabricated by drop-casting, is attributed to the H-bonds and electrostatic interactions between PEDOT:PSS and NaCMC (Figure S2, Supporting Information). In addition, the interconnected fibrils and pores are likely the result of counter-ion interactions.[28] These pores are important for the transport of water molecules due to capillary forces.[31] In addition, the H-bonding sites at the pore surface can participate in the transient interactions with water molecules, which provides the molecular basis for humidity-responsive actuation of the film at the macroscale.

In the next step, we quantify the water uptake ability of the PPC thin film via dynamic vapor sorption. After the initial drying treatment, we increase the relative humidity (RH) of the in situ chamber stepwise from 0% to 90%. The relative mass increases as a function of RH (Figure 1d). The sorption process can be divided into three stages: the first small increase from 0 to ≈7 wt.% at RH = 10% is attributed to the rapid absorption of water at hydrophilic moieties and the formation of a water layer on the internal pores of the thin film, which is followed by a linear regime up to RH = 65%, yielding a water uptake of ≈26 wt.%. This increase is related to the diffusion of water throughout the bulk film including swelling. When the RH increases from 65% to 90%, a steep rise up to a maximum of ≈76 wt.% is observed, which is attributed to the saturation of the bulk film followed by the sorption of liquid water (Figure 1d). The absorption/desorption process is not entirely reversible. We speculate that the slight hysteresis phenomenon during desorption might arise from the

deformation of the material in response to the penetration or expulsion of water.

2.3. Humidity-Responsive Mechanical Responses

Dynamic mechanical analysis (DMA) is performed at three representative RH levels (35%, 65%, 85%) to inspect the influence of humidity on the visco-elastic properties of the PPC thin film (Figure 1e). At each RH level, the samples are pre-conditioned and equilibrated prior to the DMA measurements. The storage modulus (E'') decreases from ≈4 MPa to ≈1 MPa when the RH increases from 35% to 65%. When further raising the RH to 85%, the E' decreases rapidly to ≈2 kPa. The E' decreases by a factor of 1800 from the lowest to the highest RH conditions, implying a strong mechanical response of the PPC thin film in the high RH range (65% < RH < 85%), and accordingly a high actuation performance in the moderate RH range (RH < 65%). Similarly, we analyze the changes in the loss factor (tan δ) to describe the transition of the visco-elastic properties of the thin film. A moderate increase of tan δ from 0.06 to 0.08 is observed in the RH range from 35% to 65%. When the RH further increases to 85%, tan δ grows sharply to 0.7. This finding suggests that the film becomes softer as the RH increases and that moisture weakens the H-bonding interactions among the polymer matrix. We attribute this phenomenon to the competition of H_2O molecules with the H-bonds among the components of the PPC thin film and the incurring plasticization effect. The decrease in E' with increasing RH is also in line with the DVS results, underlining the mechanical-adaptive properties of the PPC thin film.

The water absorption dynamics of the PPC thin film are further quantified by recording its volume expansion at elevated RH levels. We study the volumetric strain by tensile tests, in which the PPC thin film (20 mm in length) is fixed in the longitude direction at the testing apparatus, and the volume increase is assumed to be attributed solely to the increase in length of the film. When the RH abruptly increases from 30% to 95%, a stretching rate of 4.5 mm·min^{-1} is applied to match the length expansion of the film until the detected force turns positive. The PPC thin film becomes straight after 20 s of stretching. The calculated height expansion is 7.5%. This is a little higher than the in-plane expansion rate of the film observed from optical microscopy (5.3%), which can swell in two dimensions (Figure S3, Supporting Information). The volumetric strain is much smaller than the water absorption rate of the PPC thin film's sorption isotherms characterized by DVS. This behavior is reasonable, as although both methods investigate the water uptake ability, DVS technique detects the weight change of the film under controlled vapor pressure, and the humidity-controlled tensile testing technique detects the volume change of the film under ambient vapor pressure. When the RH decreases abruptly from 95% to 30%, the PPC thin film contracts and generates a large actuation force of 1.8 MPa, suggesting that it can reversibly expand and shrink in response to RH changes (Figure S4, Supporting Information).

2.4. Humidity-Responsive Bending Deformation

The reversible hygro-mechanical responses of the PPC thin film are highly desirable for assembling humidity-responsive actuators. When placed on a moist substrate, the PPC thin film undergoes spontaneous bending/unbending deformation (**Figure 2a–c**; Figure S5, Supporting Information). On the one hand, benefiting from the abundant sulfonate and hydroxyl groups of PEDOT:PSS and NaCMC, the exposure to water vapor induces strong H-bonding interactions between the H_2O molecules and the two components of the PPC thin film. The ensuing disruption of the original H-bonding network between PEDOT:PSS and NaCMC leads to volume expansion among the polymer chains (Figure 1b). The process described in Figure 1b takes place throughout the film regardless of the distance between the interface and the source of humidity. However, at the morphological level, the uniform lamellar structure (Figure S1, Supporting Information), which is in the in-plane direction of the film, can act as a barrier to delay the diffusion of H_2O molecules in the out-of-plane direction. Water vapor diffuses at different rates between the bottom and top surface of the film, with a higher diffusion rate at the bottom and a lower rate at the top. Therefore, a differential swelling in the out-of-plane direction of the PPC thin film is expected, inducing internal stress and resulting in an asymmetric expansion and upward bending deformation. As water evaporates, the inter- and intra-molecular H-bonds among the polymer matrix are rejoined, forcing the film to return to the unbent state. The bending/unbending deformation of the PPC thin film is reversible due to its reversibility in water adsorption/desorption.

To gain insight into the kinematic bending/unbending process, we measure the bending angle of the PPC thin film during the actuation cycle using a simplified humidity-control system. The definition of the bending angle (θ) is described in Figure S6 (Supporting Information). We observe that a strip of the PPC thin film responds within 0.15 ± 0.05 s after the exposure to water vapor, and attains a maximum bending angle of (θ = 165°) within 0.95 ± 0.07 s (Figure 2a,c; Movie S1, Supporting Information). When a PPC thin-film contacts with water vapor, the bending angle of the film varies with time, and the humidity-responsive speed of the film is fast, with the whole bending/unbending cycle taking around one second in total. Thus, neither the water uptake process nor the viscosity of the material contribute significantly to the actuation process. The actuator motion is dominated by the H-bonding interactions and the volumetric strain induced by the differential swelling, both of which depend on the RH. As a proof of concept, we assemble an athlete robot and demonstrate its weight-lifting functions in two different scenarios by using an aluminum plate as the cargo, which is 26 times heavier than the robot itself. In the first scenario, when the cargo is attached to one side of the film, the robot can lift up the cargo, and then shoot and dunk in 3.5 s (Figure 2d; Movie S2, Supporting Information). In the second scenario, when the cargo is placed in the middle of the film, the robot can grasp the cargo in 6 s (Figure 2e; Movie S2, Supporting Information). The difference in the time of execution of the robot between the first and second scenarios is due to the relative position between the cargo and the geometrical center of the film. These observations indicate the potential applications of the PPC thin films as artificial muscles.

Despite the upward bending deformation of the PPC thin film upon exposure to water vapor, ethanol, and isopropanol vapor generate a contractile force and drive the PPC thin film to bend downward (Figure 2b,c; Movie S1, Supporting Information). The solvent-responsive actuation characteristics do not change

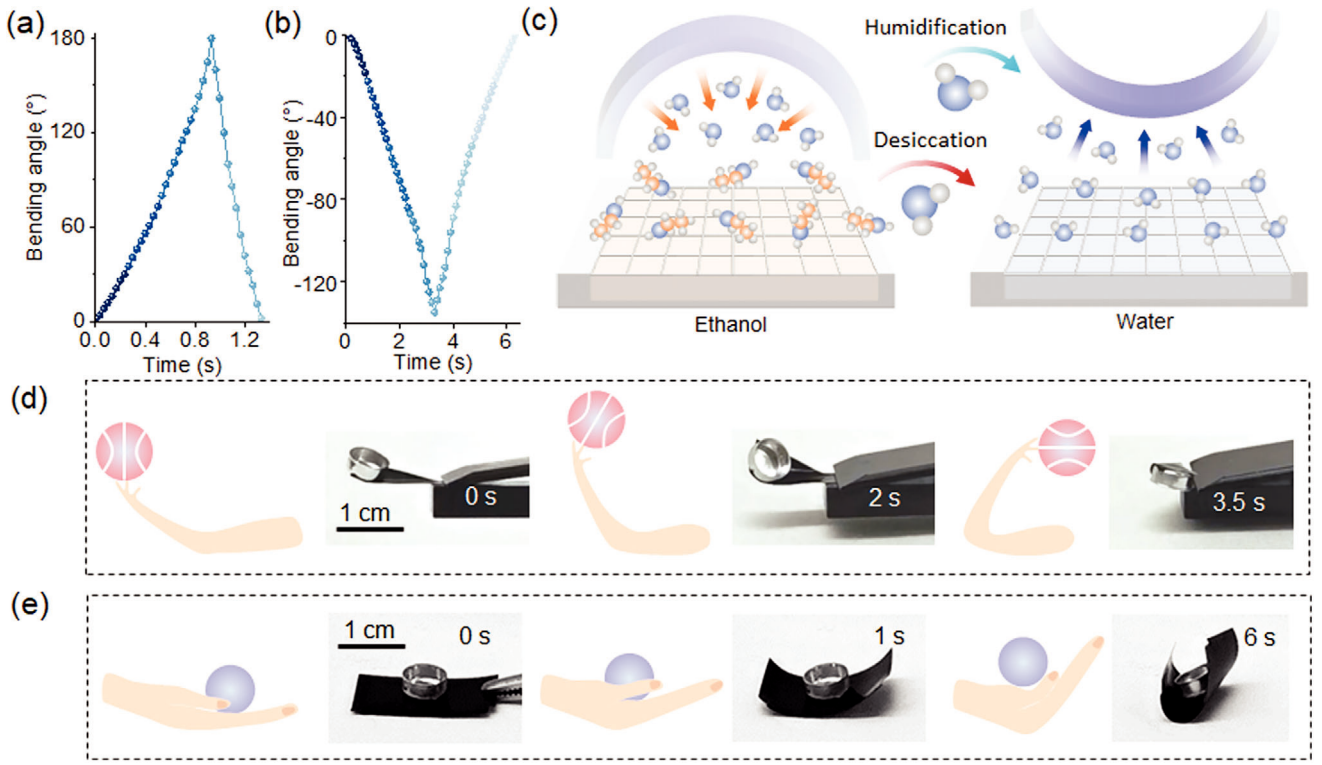

Figure 2. Actuation and robotic functions of the PPC thin film. a,b) Time-dependent variation of the bending angle of the PPC film (15 mm × 5 mm, length × width) under the influence of ethanol and water vapor. c) Schematic diagram of the actuation direction of the PPC thin film in response to vapor of water and ethanol. d,e) Proof-of-concept demonstrations of the practical applications of the athlete robot based on the PPC thin films (8 mm × 20 mm, 15 mg), which, (d) is able to lift up, shoot, and dunk a cargo (390 mg) attached to the edge of the thin film, (e) or grasp up the same cargo that is placed in the middle of the PPC film.

significantly with the type of alcohol molecules. Since the PPC thin film has a substantial fraction of hydrophilic domains, exposure to ethanol vapor promotes the desiccation of water molecules, and leads to a volume shrinkage. As the time of solvent exposure increases, the surface contraction of the PPC thin film slows down the further removal of water molecules from the interior of the film and establishes a concentration gradient across the film thickness, which drives the film to bend downward.[32] The intrinsic water inside the film is significant for the desiccation-dependent actuation of the PPC thin film in response to volatile solvents. Thus, exposure to water and ethanol vapor produces stress gradients of opposite directions.

2.5. Humidity-Responsive Electrical Properties

Inspired by the humidity-dependent conduction pathway of PEDOT:PSS from literature,[33] and our observation of the multidimensional responses of the PPC thin films to humidity variations, we investigate the influence of humidity on the electrical properties of the film. To differentiate between the electronic and ionic conduction, in situ, impedance spectra and resistivity curves are recorded while exposing the film to various RH conditions (Figure S7 and Table S1, Supporting Information). To rationally handle the complexity of the system, we focus on the influence of humidity on the resistance/impedance of the film and do not take the increased film thickness at the swollen state into account. We first measure the impedance of the PPC thin film as a function of the RH. The impedance modulus |Z| and phase angle φ of the PPC thin film are depicted as Bode diagrams in **Figure** 3a,b. The film exhibits a decreased impedance modulus as the RH increases from 25% to 90%, suggesting an improved conducting performance. Furthermore, the phase angle at 1 Hz increased from −2° at RH = 25% to −59° at RH = 90%, suggesting that the film is gaining capacitive characteristics. The overall impedance (modulus and phase) crucially depends on the RH (Figure 3c), which relates to the water content in the films as well (Figure S8, Supporting Information).

The global behavior of the film is that the impedance decreases with increasing RH, given the decreasing radius of the semicircles in the Nyquist plots in Figure 3d. At RH = 25%, the Nyquist plot of the PPC thin film shows one semicircle, suggesting that the electronic resistance is primarily the significant contribution to the impedance modulus. The Nyquist plot, with orthonormal axes, shows two semicircles at RH = 48%, including one depressed semicircle at the low-frequency range and a segmented circle at the high-frequency range, which indicates the two contributions of electronic and ionic conduction. Upon further increasing the RH to 85%, the radius of the high-frequency semicircle increases, and that of the low-frequency decreases. Thus, the impedance results suggest an electronically-dominated charge transport mechanism despite the RH variations.

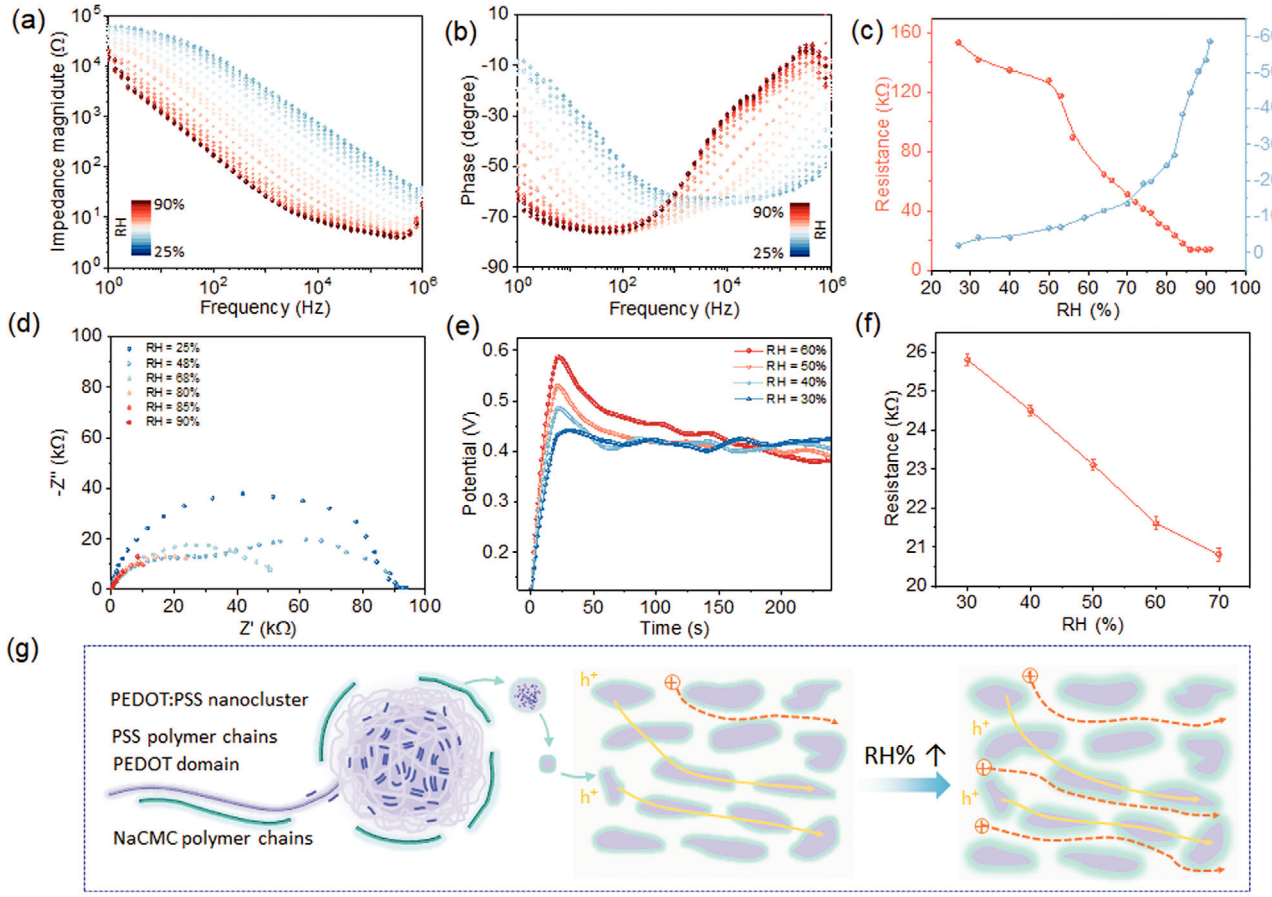

Figure 3. a) Electrical impedance modulus |Z| and b) phase plots (Bode diagrams) of the PPC thin films (size: 60 mm × 15 mm) under humidity control. For all measurements, the initial ambient RH is increased stepwise from 25% (dark blue curve) to 90% (dark red curve) over a total period of 60 min. c) Resistance and phase angle of the PPC film recorded at 1 Hz were obtained from the electrical impedance spectroscopy from (a) and (b). The curves are calibrated to the water content of the PPC film by DVS results and plotted in Figure S8 (Supporting Information). d) Nyquist plots of the PPC thin films at various RH conditions. e) Chronopotentiometry of the PPC thin film at different RH levels. f) The resistivity of the PPC thin film was calculated from the equilibrium potential from the chronopotentiometry results. For all impedance and electrical resistivity measurements, the impedance spectra or chronopotentiometry curves of three samples are tested and only one is used for analysis. g) Deduced nanostructure of PEDOT:PSS with PEDOT-rich domains embedded in a matrix of PSS and NaCMC (left). Schematic evolution of the conduction behavior within the PPC films upon the increase of the RH, with the images in the middle and right featuring the conduction behavior at the ambient and high RH levels, respectively. The yellow and dashed orange arrows depict the electronic contribution (hole transport mainly via the PEDOT domains) and ionic contribution (cation transport predominantly among the matrix of PSS and NaCMC), respectively.

As observed from the chronopotentiometry conducted at various humidity conditions (Figure 3e), the potential of the PPC thin film does not decay over time at RH = 30%, indicating the electronic contribution dominates the impedance of the PPC thin film at this humidity condition. However, when the RH increases, the potential undergoes a fast decay and then reaches an equilibrium, in which the former is caused by the flow of ionic charge carriers, and the latter originates from the electronic contribution. The trend of decay enhances at increasing RH levels. Figure 3f shows the evolution of the electronic resistivity of the PPC thin film obtained from chronopotentiometry, which decreases nearly linearly from 25.8 ± 0.2 kΩ to 20.8 ± 0.2 kΩ with the RH increases from 30% to 70%. Although the impedance modulus of the PPC thin film changes by roughly one order of magnitude up in the entire RH range, the resistance of the film decreases only by ≈19% over this RH range, suggesting the important role of ionic contribution. The resistivity values differ from each other because the impedance measurement is based on alternate current (AC) excitation (here at 1 Hz), whereas the chronopotentiometry is a direct current (DC) method. The potential of tuning the conduction mode of the PPC thin film via RH control can be used to precisely inspect the environmental RH conditions via real-time transduction of electrical signals.

Combining the information from the electroanalytical in situ investigations, we divide the humidity-responsive ionic conduction behavior of the PPC thin film into the following stages (Figure 3g). At the beginning (RH = 25%), the PEDOT:PSS/NaCMC composite is maintained by the core-shell arrangement of insulating PSS chains and the conducting PEDOT oligomers, and the counter-ion interactions of PSS^- and Na^+CMC. This structure leads to a high impedance modulus |Z|. In the low RH range (25% < RH < 55%), the polyelectrolyte

nature of PSS^- and humidity-responsive swelling of the film leads to a dissociation of ions and the formation of solvation shells. An ionic contribution of charge transfer is detected from electrical impedance spectroscopy, which potentially arises from two sources. On the one hand, water molecules solvate the sulfonate groups in the immobile PSS chains, which leads to the screening of the electrostatic attractions between PSS^- toward the cations, and thus an easier cation transport through the PSS matrix.[34] On the other hand, as we learn from the DMA tests, the PPC thin film gets plasticized by water upon hydration, which enables a higher chain mobility. The ionic contribution leads to a strong decrease in impedance modulus upon RH increases. In the high RH range (55% < RH < 85%), the impedance modulus increases, suggesting that water molecules form multiple solvation shells contribute, which continue to enhance ion conduction. The impedance modulus reaches a plateau when the RH further increases to 90%, indicating a weaker influence of RH on the ion conduction. The first two regions of the evolution of impedance coincide with the trend, which we observe from the DMA results.

The electronic resistivity of the PPC thin film also decreases with RH but is less RH-dependent compared to the ionic counterpart. This behavior contributes to the influence of humidity on the structural rearrangement of the PPC film, which affects the arrangement of the PEDOT percolation network. A likely reason is that an increased interconnection of the PEDOT-rich domains is achieved, which enhances the electronic transport among the inter-domains of PEDOT.[22] Another reason can be that the solvation of the PSS shells reduces the electrostatic traps for the electronic holes of $PEDOT^+$, and the mobility of holes reduces the electronic resistivity.

2.6. Micro-Morphologies Due to Injury-Induced Deformation

To simulate mechanical damages and study the humidity-induced healing capability of the PPC thin film, two strips of PPC thin films are either pierced with a needle to prepare a punctured sample (Type I) or stretched beyond the yielding point at a tensile testing machine to prepare an over-stretched sample (Type II, **Figure** 4a), respectively. Due to the densely packed lamellar structure and multiple H-bonded networks, the PPC thin film shows outstanding tensile strength. From the representative strain-stress curves (Figure S9, Supporting Information), we observe a good comprehensive mechanical property, with a tensile strength of 12 ± 1 MPa and a fracture strain of 426 ± 22%. Increasing the content of NaCMC would decrease the tensile strength but greatly increase the fracture strain of the PPC thin film. This behavior indicates that the rigid PEDOT:PSS scaffold not only acts as a reinforcement but also participates in the assembly of the H-bonded crosslinking network. These non-covalent interactions contribute to a robust microstructure, which further results in enhanced mechanical load transfer and energy dissipation ability.

For both mechanically damaged samples, the PPC thin film unveils a typical plastic deformation character (Figure 4b). Although the injury has been forced in the out-of-plane direction, the morphological changes created by the Type I injury are in the radial directions parallel to the film surface with a relatively small injured area, and with a sharp gradient in the size and distribution of the injury-induced microstructures (Figure 4b-i,ii). The distribution of the structures becomes denser, and the size of the structures becomes smaller when the scan position approaches the injury center. In the Type II sample, the injury-induced morphological changes are uniformly distributed parallel to the film surface. Therefore, the Type I sample can be locally regarded as a miniature of the Type II (Table S2, Supporting Information). The injury-induced microscale morphology of the samples is analyzed by cross-sectional SEM analysis. Three microstructures can be identified, including ruptured fibrils, spheres, and nano to microscale cavities, which typically represent the multiple-crazing and yielding behavior (Figure 4b-iii,iv). The length of cavities is in the range of several hundred nanometers, which is within the wavelengths of visible light and leads to strong stress whitening.[35] The spheres originate from fractured fibrils, since they are absent in the samples before being injured, and are distributed in between the fibrils in both types of samples (Figure 4b; Figure S1, Supporting Information).

2.7. Probing the Injury-Induced Microstructures with X-Ray Scattering

Inspired by the swelling-induced volume expansion and H-bond destruction/reconstruction in the wetted area of the PPC thin film, we anticipate that the microscale injuries of the PPC thin film can recover by humidifying. Therefore, the evolution of the injury-induced microstructures at the fractured surface of the PPC thin film is examined by USAXS under humidity control. USAXS allows for detecting the multi-crazing behavior due to its ability to access the strong difference in electron density between the polymer matrix and the cavities in the relevant angular range.[35] Specifically, these measurements allow for the extraction of geometrical parameters of structures at the nano- and sub-microscale, such as the size of the cavities. To study the humidity-induced healing of the PPC thin film, USAXS measurements are conducted at the P03 beamline of PETRA III (Deutsches Elektronen-Synchrotron DESY).[36] The setup of an in situ USAXS experiment with humidity control is shown in Figure 4c and Figure S10 (Supporting Information). A strip of injured samples is fixed in the custom-built humidity cell.[37] The RH of the cell is programmed to vary stepwise from 0% to 100%, and then from 100% to 0% with the increase/decrease at each step being 10%, and kept for 5 min, giving 21 steps in total (Figures S10 and S11, Supporting Information). The RH cycle can be divided into a humidifying (RH increase, p) and a drying (RH decrease, n) process. The samples are scanned in *z*-direction to compare the structural variations due to different degrees of injury-induced deformation.

We first look into the 2D USAXS data of both mechanically damaged samples at RH = 0% (Figure 4d). In either type of sample, the non-injured area shows a weak and isotropic scattering pattern, indicating the absence of structural inhomogeneity (Figure S12, Supporting Information). As the scan position of X-ray approaches the injured area of the type I sample, the scattering pattern evolves into an elliptical shape, with intensified scattering in both the equatorial and meridional directions, which is assigned with the formation of highly-oriented fibrils and

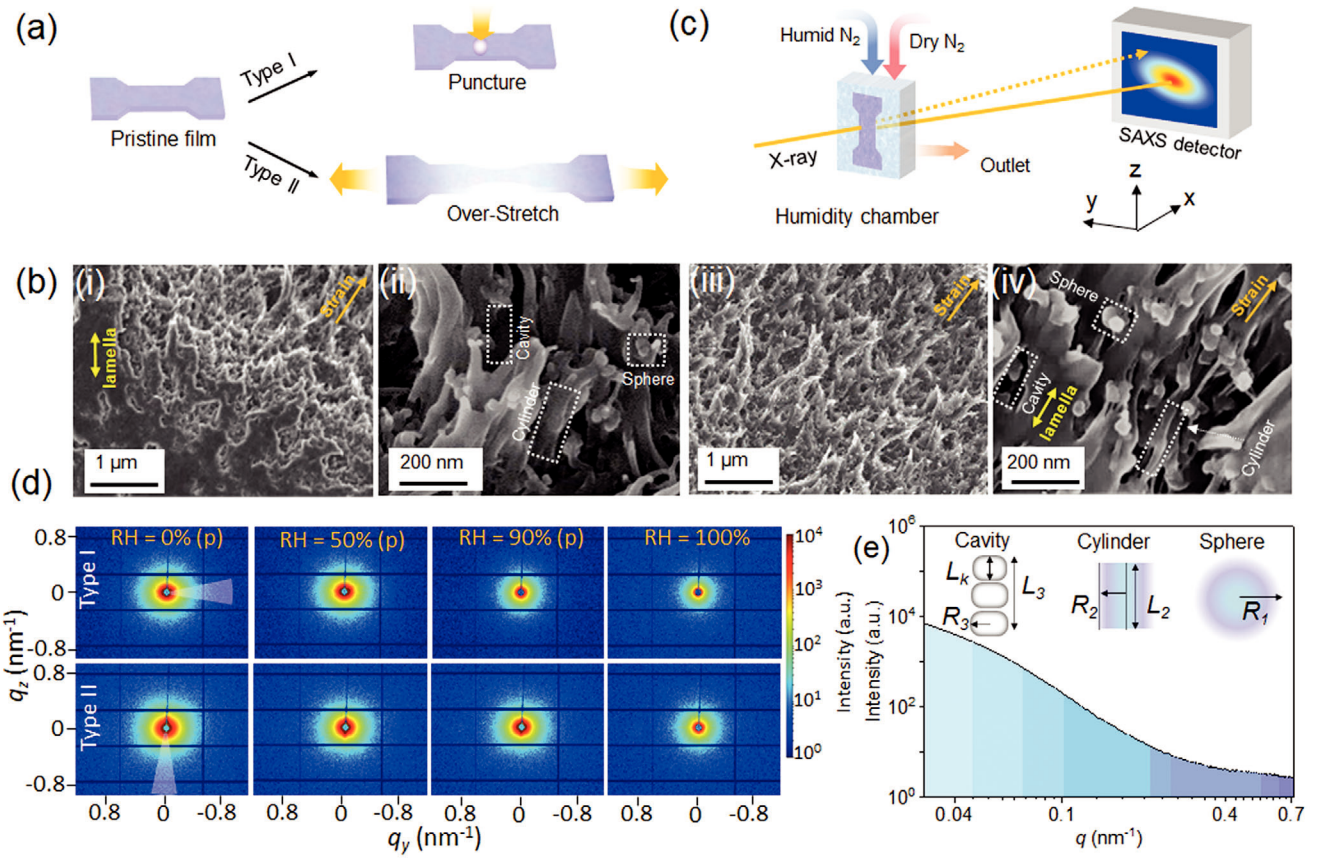

Figure 4. Structure analysis of the microstructural evolution of the injured PPC thin films under humidity control. a) Schematic of the fabrication of the injured samples, including puncturing (Type I, local injury) and over-stretching (Type II, uniform injury), respectively. The yellow arrows depict the direction of injury with respect to the in-plane direction of the PPC thin films. The size of the scanned area for both types of samples is 10 mm × 2 mm. b) Cross-sectional SEM images at the injured area of the Type I (left, (i) & (ii)) and Type II (right (iii) & (iv)) samples. c) Layout of the USAXS experiment. The samples are fixed in a humidity-controlled chamber.[38] The humidity is varied to increase from 0% to 100% (humidifying) and decrease to 0% again (drying) through the circulation of a mixture of humid and dry nitrogen gas USAXS data are collected during the humidifying/drying cycle. d) Representative USAXS data of Type I (top panel) and II (bottom panel) samples at the center of the injured area during the humidifying process. "p" denotes the humidifying part of the humidifying/drying cycle (abbreviation of "positive"). The USAXS images at RH of 0% (p), 50% (p), 90% (p) and 100% are shown. The 2D USAXS images are integrated at the dashed areas to obtain the 1D scattering curve. A representative 1D curve of the Type II sample is plotted in e). The area under the curve was marked by distinct colors at the high-q, middle-q, and low-q regions, to differentiate among the three geometrical objects that are used to fit the data. A structural model with these three geometrical objects and the relevant structural parameters used for least-square-fits to the USAXS data, including the radius of the sphere (R_1), radius (R_2) and length (L_2) of the cylinder, radius (R_3), Kuhn length (L_k) and contour length (L_3) of the cavity.

cavities with close proximity (Figure S13, Supporting Information). When RH increases from 0% to 50%, the scattering pattern at a fixed location remains nearly unchanged in both types of samples. However, an attenuation of scattering intensity and a change of the scattering pattern from an elliptical to a circular shape is observed as RH increases from 50% to 90% at the injured area of the Type I sample, which indicates the reduction of the number or size of anisotropic microstructures. When RH further increases to 100%, a nearly isotropic scattering pattern is observed and the scattering intensity gradually attenuates as the RH decreases to 0%. Moreover, the whitened region in the Type I and II samples become transparent after the humidifying/drying treatment, suggesting the diminishing of the anisotropic microstructures due to humidity-induced rearrangement of the polymer matrix along with volume shrinkage of the cavities.

2.8. Modeling the Humidity-Induced Structural Rearrangement

To study the recovery of the microstructural injuries of the PPC thin film under the influence of RH variations in detail, we perform azimuthal cuts and analyze the resulting 1D USAXS data. The 1D profiles of the PPC thin film are divided into three q regions: the low-q region ($0.03 < q < 0.1$ nm^{-1}) featuring the cavities at the sub-microscale,[39] the mid-q region ($0.1 < q < 0.29$ nm^{-1}) representing fibrous polymer matrix, and the high-q region ($0.29 < q < 0.7$ nm^{-1}) reflecting spherical objects, (Figure 4e). It is worth mentioning that the scattering curves at different scan positions across the Type II sample are nearly identical, but vary significantly in the Type I sample (Figure S14, Supporting Information). In the Type II sample, the broad peak at the low-q region is universally distributed over all scan positions. In the Type I sample, the scattering profile at the non-injured part (scan

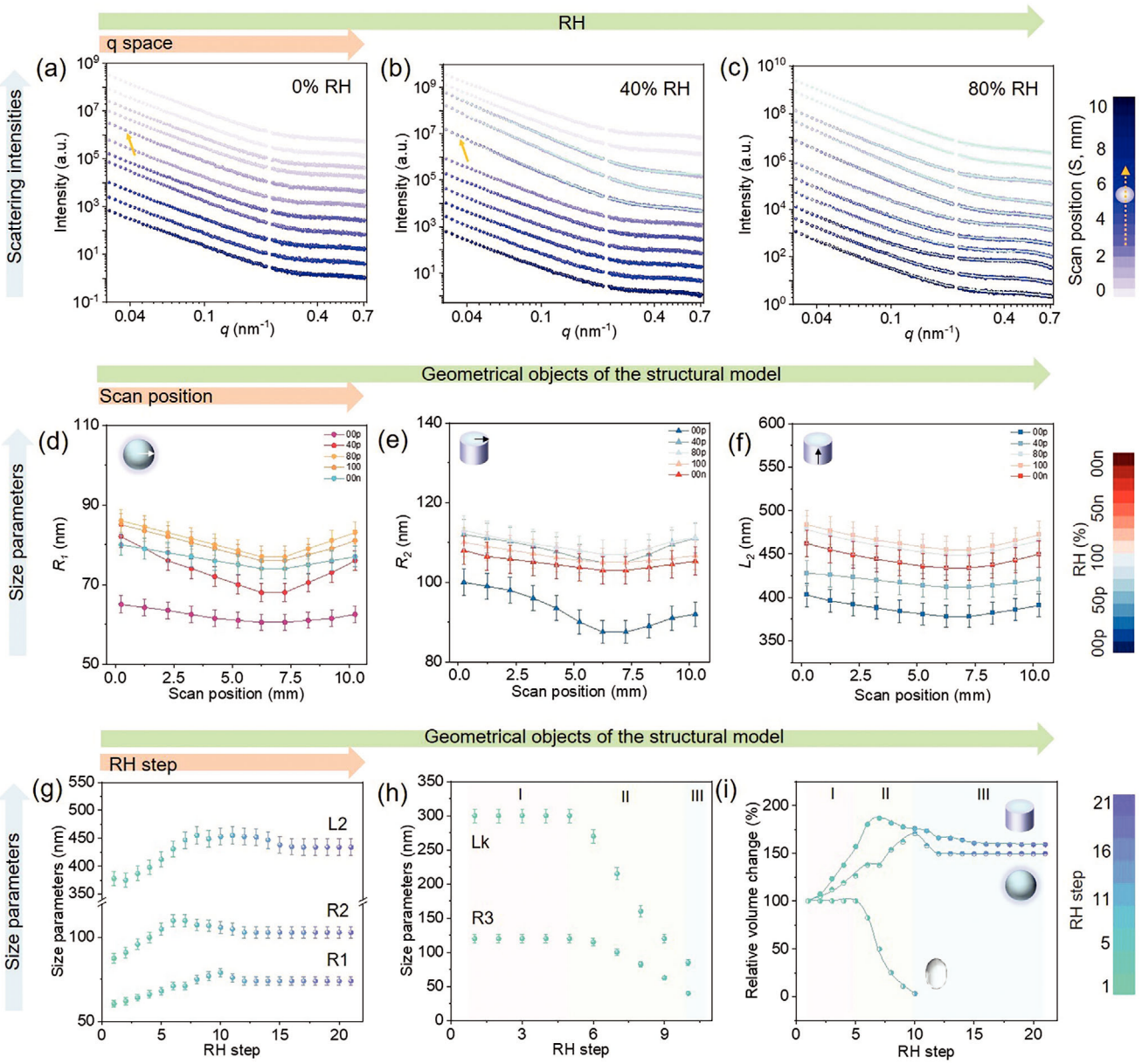

Figure 5. Humidity-induced structural rearrangement of the injured PPC thin film. a–c) 1D USAXS data (the colors of the symbols correspond to the scattering data measured at different RH levels) and fits (solid lines, light blue) collected along the longitude of the Type I sample at RH of 0% (a, dry state), 40% (b, swelling state), and 80% (c, saturation state). The yellow arrows guide to the eye the shift of the peak at $q = 0.06$ nm^{-1} to the low-q region. d–f) Representative fit parameters of the objects of the structural model at the center of injury in the Type I sample during the humidifying/drying cycle, including the radius of the sphere (d), radius (e) and (f) length of the cylinder. The size parameters are depicted in the up-left corner of each figure correspondingly. The values of size parameters are marked with distinct colors, which correspond to the RH levels at which the USAXS data are collected. g,h) Evolution of the fit parameters at the center of injury, with (g) corresponding to the parameters of the sphere and cylinder, and (h) corresponding to the cavity. i) Ratio of the volume of the three objects compared to their initial value with respect to the RH steps. For cavities, the volume of a single unit of flexible cylinder is used for analysis. The three stages of the structural evolution of cavities are marked with shadowed areas with different colors in (h) and (i).

position, $S = 0$ mm) shows a relatively flat curve in the high-q region and a featureless slope in the mid-q region, suggesting a homogeneous distribution of the supramolecular network. However, a peak at $q = 0.06$ nm^{-1} emerges and slightly shifts to the low-q region as the beam approaches the center of injury ($S = 6$ mm, **Figure** 5a,b). The increased intensity at the low-q region is caused by a high scattering contrast, due to the stretching-induced cavities and/or fibrils.[39] This observation agrees well with the SEM micrographs, which display a morphology composed of spheres, and interconnected fibrils in conjunction with a series of cavities.

We thus adopt a fit to the USAXS data using three nanoscale objects, namely sphere, cylinder, and flexible cylinder (abbreviated as "cavity", Figure 4e). It should be noted that the sphere model is at the sub-microscale and is different from that of the "core-shell sphere" structure for interpreting the electric properties of PEDOT:PSS, the latter of which is normally at the nanoscale outside of the USAXS range probed here.[40] The least-square fits of the geometrical models to the USAXS data allow us to extract physically relevant and quantitative structural parameters with high statistical significance, which we compare with the structures seen in the electron micrographs. Therefore, SEM image information is used as constraints for the parameters in the fits including the shape and size of the structures. We use a fit procedure as described in the literature.[41] Calculation of the X-ray scattering length density (SLD) for each model is described in the Experimental Section. The polydispersity of size parameters representing the polymer network manifests in a smearing of the scattering pattern. We account for this non-uniformity by applying a Gaussian size distribution in the modeling/fitting. To reduce the complexity of the USAXS data analysis, only the size parameters, including the radius (R) and length (L) of the models, are used for analysis. The polydispersity we used for the length of the cylinder and cavity is 0.1, and for radius of the three objects is 0.05. A typical fit procedure is described in Figure S15 (Supporting Information). The best fits of the scattering curve are shown in Figure 5a–c. The relationship between the structural parameters of the sphere (R_1), cylinder (R_2, L_2), cavity (R_3, L_3, L_k), and the relative humidity (RH step), as well as the scan position (S), are displayed in Figure 5d,e; Figure S16 (Supporting Information) (Type I samples) and Figure S17 (Supporting Information) (Type II samples), respectively.

Due to the homogeneous chemical composition of the PPC thin film, we assume that the cylinder and the sphere model have the same chemical composition of PEDOT:PSS scaffold entangled with the NaCMC matrix. This assumption is supported by the granular and fibrillary structures observed in Figure 4b. The cylinder model manifests the elongation of the polymer network, and the sphere model describes the residual of the fractured polymer matrix after injury. The variation of parameters of the sphere and cylinder models in the Type I sample is significantly stronger than in the Type II sample, see Figures S16 and S17 (Supporting Information). Therefore, we mainly focus on the Type I sample to study the injury-induced nanoscale changes. For spheres, the radius R_1 decreases from (R_1 = 65 ± 4 nm) to (R_1 = 60 ± 4 nm) when the scan position approaches the center of injury (S = 6 mm). For cylinders, the evolution of R_2, L_2 is nearly consistent with the spheres. For example, from S = 0 mm to S = 6 mm, the radius R_2 drop nearly linearly from (R_2 = 100 ± 5 nm) to (R_2 = 88 ± 6 nm) at RH = 100%. The similar evolution mode of the fit parameters of the spheres and cylinders qualitatively reflects the elongation of the entangled polymeric network. The length of the cylinder also decreases slightly from (L_2 = 351 ± 14 nm) to (L_2 = 328 ± 14 nm) as the scan position moves to the center of injury. The residual of the polymer matrix which is fractured from the end of fibrils reduces its aspect ratio, indicating a preferable formation of a sphere-like shape.

In the next part, we study the variation of the spheres and cylinders of the Type I sample in the humidifying/drying cycle (Figure 5d–f; Figure S16, Supporting Information). At the center of injury, the radius of spheres increases from (R_1 = 60 ± 4 nm) at RH = 0% to (R_1 = 71 ± 5 nm) at RH = 50% and further expands to (R_1 = 79 ± 5 nm) at RH = 100%. When the RH decreases from 100% to 0%, only a small decrease (R_1 = 74 ± 5 nm) at RH = 0% is observed (Figure 5d). Second, the size of the cylinder increases at the beginning of the humidifying process from (R_2 = 88 ± 6 nm) at RH = 0% to (R_2 = 96 ± 7 nm) at RH = 50% due to the swelling of the oriented polymer matrix and then decreases slightly from R_2 = 110 ± 8 nm (RH = 50%) to R_2 = 103 ± 7 nm (RH = 100%). This change may relate to the over-swelling of the oriented polymer matrix, which softens and eventually fragments when getting into contact with the adjacent fibers at a high RH (Figure 5e). The length of cylinders shows a sharp increase similar to the radius of the cylinders at the initial humidifying stage from (L_2 = 378 ± 14 nm) at RH = 0% to (L_2 = 431 ± 17 nm) at RH = 50% due to swelling of the matrix (Figure 5f,g). When the RH further increases to 100%, the fibrils rejoin and reattach driven by capillary forces, which leads to a slight increase in the length of cylinders to (L_2 = 453 ± 21 nm). The slight increase in the length of cylinders may also be attributed to the re-attachment of the swollen spheres. This behavior also coincides with the poor mechanical properties of the PPC thin film at a high RH (85%), which is 541 times lower than that measured at RH = 65% (Figure 1e). The length of cylinders remains at (L_2 = 447 ± 20 nm) when the RH decreases from 90% to 0%.

The cavities exist but only with a small number fraction in the Type I sample. Therefore, we mainly focus on the Type II sample to investigate the evolution of cavities, since strain-induced whitening is the main structural feature of them. The cavities are described by the third component in the fits – the flexible cylinder – which is illustrated as a chain of segmented units.[39] Humidity-dependent variation of the radius and length of the unit cavity (R_3, L_k) is shown in Figure S17 (Supporting Information). The total length (L_3) is defined as the contour length and the Kuhn length (L_k) is the length of a single unit. As the scan position moves toward S = 6 mm at RH = 0%, the radius and length of cavities, and contour length remain constant, with (R_3 = 120 ± 6 nm), (L_k = 300 ± 15 nm) and (L_3 = 1300 ± 65 nm). This trend is explained by the uniform distribution of structural features in the Type II sample (Figure 5h). We divide the evolution of cavities in the Type II sample into three RH stages. The size parameters of the spheres, cylinders, and cavities remain constant from RH = 0% to RH = 30% (Stage I). Then the parameters of spheres and cylinders increase sharply from RH = 30% to RH = 60% with a dramatic decrease in the size parameters of cavities (Stage II, Figure S17a–c, Supporting Information). In the rest of the humidifying/drying cycle, the spheres and cylinders display only a slight decrease in their size parameters, while the cavities become nearly undetectable due to their low scattering densities (Stage III). For example, the radius of the cavity remains at (R_3 = 120 ± 6 nm) from RH = 0% to RH = 30% and decreases almost linearly to (R_3 = 22 ± 1 nm) at RH = 60% (Figure S17d, Supporting Information). The Kuhn length manifests a similar evolution trend, which remains unchanged at (L_k = 300 ± 15 nm) when RH increases from 0% to 30% and decreases sharply to (L_k = 55 ± 3 nm) when RH increases to 60% (green shadowed area in Figure S17e, Supporting Information). In the remaining steps of the cycle, the radius and Kuhn length of the cavities further evolve beyond the

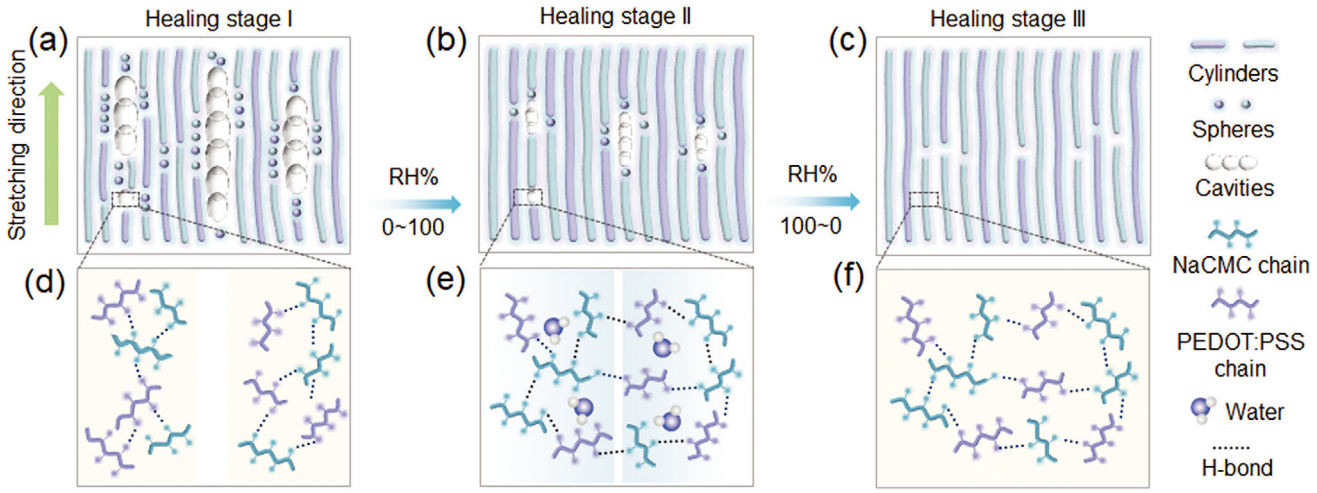

Figure 6. Schematic of the structural evolution of the PPC thin film during the humidifying/drying cycle deduced from the results of FTIR, SEM, and USAXS. The structural evolution of the PPC thin film is divided into three stages (Stage I: a,d; Stage II: b,e; Stage III: c,f) according to the results in Figure 5h. The structural evolution is deduced at the microscale a–c) and the molecular scale d–f), respectively.

detectable *q*-range of USAXS measurement. The evolution of the spheres and cylinders is in accordance with those in the Type I sample and opposite to the trend of cavities. The volume shrinkage, or the closure of cavities in the Type II sample – seen by the reduction of R_3 and L_k – indicates the healing of microscale injuries.

Based on these results, it is inferred that humidity not only plays a critical role in regulating the supramolecular network, but also in the rearrangement of the microstructures of the PPC thin film (Table S3, Supporting Information). Therefore, we propose the necessary steps for the humidity-induced structural rearrangement of the PPC thin film deduced from the structural information by USAXS (Figure 5i) and reconstruction of the H-bonded supramolecular network by FTIR (Figure 1c). In the dry state, the surface of the sub-micrometer-sized cavities possesses abundant hydroxyl and carboxyl groups available for H-bonding. These spaces can be effectively filled by water molecules, which saturate the H-bonds. In the first step, the PPC thin film absorbs a large amount of water at a relatively low RH level. This behavior is supported by the USAXS results, where the volume of the flexible cylinder remains stable despite the increase of RH at this stage, which suggests that the polymer network does not extensively swell and grow in size. Meanwhile, the size parameters of the sphere and cylinder only slightly grow (**Figure** 6a,d). The second step is the extensive swelling of the polymer matrix, which accounts for the increase in size parameters of the sphere and cylinder and the decrease in that of the cavities (Figure 6b).[39] Water molecules that penetrate into the film dissociate the original H-bonds. Moreover, the water-plasticization of polymers decreases the glass transition temperature of polymers to below the room temperature – in comparison to the dry state, thus giving access to higher chain mobility for structural rearrangement.[42] Besides, the swelling-induced volume expansion and capillary force bring the polymer chains at the freshly fractured surface closely together, which is important for the reconstruction of the H-bonded supramolecular network since H-bonds are short-ranged and require direct contact to form (Figure 6e). In the third step, water molecules desorb from the film, resulting in the re-exposure of the hydroxyl and carboxyl groups of the polymer chains that formed H-bonds with water in the second step. Therefore, the inter- and intra-molecular H-bonding among PEDOT:PSS and NaCMC at the fractured interface reformed (Figure 6f). Simultaneously, desorption also reduces the mobility of polymer chains in the spheres and cavities and stabilizes the volume of the cavities (Figure 6c). These dynamic processes give access to the healing of the injury-induced microstructures via humidity-induced structural rearrangement at multi-length scales.

Besides, there are three factors that we shall take into account. 1) The injury-induced cavities at the sub-microscale that exhibit abundant H-bonding groups shall be distinguished from the evaporation-induced pores created at the film preparation steps, which are essential for humidity-responsive actuation performance. The surface of these pores has a lower concentration of H-bonding groups compared to the newly-fractured cavities.[39] However, both the cavities and pores contribute to the humidity-responsiveness of the thin film. 2) The non-injured part of the PPC thin film can retain its microstructures after the humidifying/drying treatment, which reveals that the part with a lower exposure degree of the H-bonding sites (due to injuries) is not significantly disrupted during the healing process. Thus the mechanical integrity of the film is well preserved. This is an advantage since the injured part of the material will be preferentially repaired due to the higher exposure of the H-bonding groups and the prolonged retention of water. 3) Since the H-bonded network can be readily regenerated with the aid of water, the humidity-responsiveness of the PPC thin film not only allows efficient sensing, and actuating but also healing capabilities. The unique humidity-responsive supramolecular network of the PPC thin film is mechanically strong to generate an actuation deformation at a moderate RH, but its supramolecular network can be easily switched to a soft state at a high RH to perform healing of the nano- to micro-scale injuries.

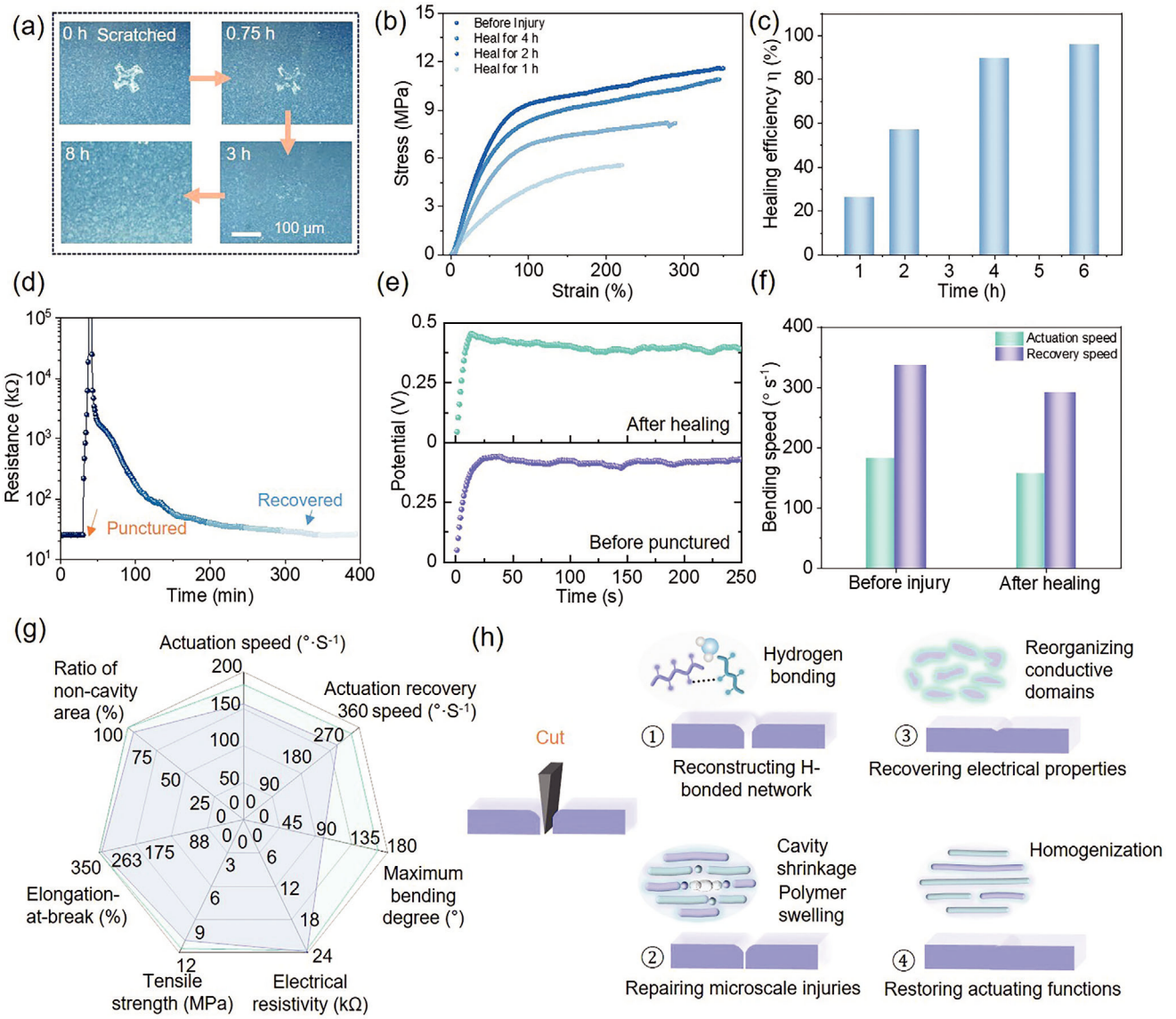

Figure 7. a) Optical microscopic images showing the humidity-induced healing of the PPC thin film at the ambient condition (T = 25 °C, RH = 50%). b) Comparison of the strain-stress curves of the non-injured and healed PPC thin films after different healing durations. c) The healing efficiency of the PPC thin film is calculated from the strain-stress curves. d) Resistivity curve of the PPC thin film during the healing process in the ambient condition (T = 25 °C, RH = 50%). The sample has been bisected with a razor blade, and the orange arrow depicts the time of bisection. e) Chronopotentiometry curves of a non-injured (bottom) and a healed (top) PPC thin film. f) Comparison of the actuation and recovery speed of the PPC thin film in response to humidity variations before (left) and after (right) healing. g) Comparison of the efficiency of healing of the PPC film in terms of the ratio of non-cavity-area, elongation at break, tensile strength, electrical resistivity, maximum actuation bending angle, actuation bending, and unbending speed. h) Deduction of the mechanism of the healing of the PPC thin film at different length scales and functional levels.

2.9. Humidity-Induced Recovery of the Mechanical, Electrical, and Actuating Functions

Although the PPC thin film does not directly exhibit a self-healing property in ambient conditions (T = 25 °C, RH = 30%), it achieves a healing capability assisted by rearranging the microstructures and the H-bonded supramolecular network by humidifying. A scratch made by a steel screwdriver with a depth of 100 μm of the PPC thin film is completely repaired after 8 h at the ambient condition (T = 25 °C, RH = 50%) (**Figure 7a**). The humidity-induced healing process recovers not only the damaged morphology but also the mechanical properties. The strain-stress curves indicate that the mechanical performance of the PPC thin film recovers gradually with the time of healing (Figure 7b). After 4 h, the scratched sample restores its toughness with a healing efficiency of 96% (Figure 7c). Simultaneously, we monitor the restoration of the electrical properties of the PPC thin film through DC resistivity curves. The full recovery (5.8 h) of the conduction behavior of the PPC thin film takes a longer time (Figure 7d) than that of the recovery of toughness (4 h) in

samples with the same type of mechanical injury. This phenomenon results from interfacial and entropic energy as drivers of the healing of the injury-induced microstructures. Hence, significant portions of the electrical property become recovered only after the scratch is completely healed, which is unnecessary for the full recovery of toughness. Moreover, chronopotentiometry curves of the healed PPC thin film are recorded. The resistivity of the healed PPC film recovers to ≈26 kΩ, which is slightly higher than that of the non-injured sample (≈24 kΩ). A slight decay of the potential at the beginning of the measurement is observed, which arises from the slightly higher water content of the film after healing due to the remaining water inside the film after the humidifying/drying treatment (Figure 7e). These results indicate that the PPC thin film has restored sufficient humidity-responsive mechanical and electrical properties, which benefits the durability of the actuator in a humid application environment.

Soft actuators are inevitably subjected to microscale injuries and cracks during operation, thus the healing capacity is of vital importance for the actuators to maintain an extended service life. The healing capability of the PPC thin film is also validated by studying the recovery of its actuating properties. To intuitively demonstrate the recovery of the actuating function, we cut the PPC thin film and examined its actuation speed after the humidifying/drying treatment. The healed film resumes its operation and performs bending deformation with an actuation speed of 157 °·s^{-1} (Figure 7f), which is only a little slower compared to the pristine one (180 °·s^{-1}). The calculated healing efficiency is 85% by dividing the actuating speed of the healed sample by that of the non-injured sample (Movie S3, Supporting Information). We compared the healing performance of the PPC thin film in terms of the recovery of the injury-related microstructures, humidity-responsive actuation performance, mechanical properties, and electrical resistivity under the same humidifying-drying treatment (Figure 7g). Generally, the healing efficiency is the highest in the repairing of injury-related microstructures, followed by restoration of mechanical performance, electrical resistivity, and finally the recovery of the actuation performance (Figure 7h). Although the sensitivity of the actuator (bending speed) is only slightly deteriorated due to the reconstruction of the hydrogen-bonded network, the actuation amplitude (maximum bending angle) is reduced to 60% of the original value. Thus, the recovery of the actuation performance requires the homogenization of the polymer matrix despite the full recovery of the mechanical performance.

Compared to room-temperature self-healing materials, the softening of the PPC thin film can be controlled by exposure to moisture, which also ensures the mechanical stability and durability of the devices fabricated on the basis of the PPC thin film in its ambient working conditions. The actuation and healing capacity of the PPC thin film depends on the same structural basis and the same type of energy input (humidity in this case), which triggers reversible structural rearrangement of the film at multiple length scales. The structural rearrangement proceeds faster for films with a uniform morphology, which is observed in the form of actuation. However, it proceeds relatively slower in a fractured film, since more functional groups are exposed and prolong their interactions with moisture, which is observed in the form of healing.

Actuation deformation requires a quick release of potential energy and propagation of the humidity-induced structural changes across the PPC thin film as it becomes saturated with moisture. Healing, on the other hand, requires the relatively slower release of potential energy and the non-intervened repairing of microstructures at the interface of local damage. We demonstrate the feasibility of a general design strategy of healable actuators, of which the platform can be broadened by incorporating a variety of stimuli-responsive elements that continuously transform the potential energy of environmental stimuli into kinetic energy. Besides, the PPC thin film can be exploited as coating or hosting materials for the other stimuli-responsive elements in more diverse multi-component systems.

3. Conclusion

In summary, we develop a structurally-rearrangeable thin film, in which the structural, mechanical, and electrical properties of the film can be regulated by varying the humidity conditions. Owing to the supramolecular network of PEDOT:PSS and NaCMC through physical crosslinking and hydrogen bonding, the PPC thin film exhibits excellent actuating performance and an efficient healing ability of both the microstructures and functionalities. As a proof of concept, we fabricate an athlete robot, which performs humidity-induced cargo-lifting and grasping functions. Our dynamic crosslinking design provides an effective strategy to solve the inherent conflict between stimuli-responsive actuation and healing. It is worth emphasizing that although significant advances have been made in assembling self-healing actuators, this work is among the first in situ investigations on the humidity-controlled microstructural, mechanical, and electrical properties of a healable actuator with switchable healing and actuation capacity. Based on these achievements, we anticipate that this design platform holds great promise in the scalable production of stimuli-responsive thin films, and in applications wherever the environmental conditions play a role in regulating the properties of structurally rearrangeable materials, such as artificial muscles, soft robotics, or environmental condition monitoring.

4. Experimental Section

Materials and Film Preparation: Poly(3,4-ethylenedioxythiophene):poly(styrenesulfonate) (PEDOT:PSS, CAS No. 155090-83-8) water dispersion and sodium carboxymethyl cellulose (NaCMC, average Mw of 700000, CAS No. 9004-32-4) was purchased from Sigma-Aldrich and used as received. 2.5 g of NaCMC powder was dissolved in 10 mL of diH_2O, heated at 120 °C for 0.5 h, and cooled down at 25 °C to prepare the 25 wt.% NaCMC water solution. The water dispersion of PEDOT:PSS (1.1 wt.%) and NaCMC (2.5 wt.%) solution were mixed with a weight ratio of 4:1 and stirred vigorously at 700 rpm for 10 min. The mixture was cast onto a pre-cleaned glass slide and dried at the ambient condition (T = 25 °C, RH = 30%) for 8 h, resulting in a dark blue film adhering tightly to the slide.

Hydrogen/Deuterium (H/D) Exchange Fourier Transform Infrared Spectroscopy (FTIR): The FTIR spectra of the PPC thin film were recorded at ambient conditions (T = 25 °C, RH = 30%). The reflectance infrared spectra were collected through a Bruker Vector 22 spectrometer with a diamond cell attenuated total reflection (ATR) accessory module in the range of 800–4000 cm^{-1}. The thin film was soaked in D_2O for 20 s, and the excess D_2O was removed from the film surface before the measurement. FTIR spectra were scanned once per minute, and each scan took 40 s.

Dynamic Vapor Sorption Analysis: Dynamic water vapor adsorption and desorption were measured by an automated sorption balance device (DVS Advantage ET85, Surface Measurement Systems Ltd., USA). A total of 10 mg of PPC thin film (weighted at T = 25 °C, RH = 50%) was dried for 6 h at 60 °C and at a partial water vapor pressure of $p/p_0 = 0$. The film was exposed to ascending p/p_0 steps of 0, 0.05, 0.10, 0.15, 0.20, 0.25, 0.30, 0.40, 0.60, 0.80, 0.85, 0.90, 0.95, and 0.98 for adsorption and then descending in the same manner for desorption. The samples were exposed to a flow rate of 200 SCCM, and the carrier gas was N_2.

Dynamic Mechanical Analysis: Humidity-responsive visco-elastic behavior of the PPC thin film was performed on a DMA Q800 device with a DMA-RH Accessory (TA Instruments, New Castle, Delaware, USA), which allows mechanical properties of a sample to be analyzed under varying RH conditions. Free-standing PPC thin films (length × width: 60 mm × 8 mm) were pre-conditioned at a constant temperature of 25 °C and a high RH (85%), ambient RH (65%), and low RH (35%). After the sample was placed in tension between a fixed and moveable clamp, the RH chamber was closed to obtain the desired RH. RH was increased stepwise with a waiting time of 0.5–2 h for equilibration of the samples between the individual steps, and the sample was scanned at three given RHs for 80 min. All tests were conducted at a frequency of 1 Hz and a linear range of 0.5% strain. Three separate measurements were taken to generate an average DMA result. The data was acquired by Orchestrator v7.2.0.4 software.

Humidity-Induced Internal Stress: The humidity-responsive swelling of the PPC thin film was measured with a Zwick Z005 testing machine. By clamping the sample at the tensile tester, the volumetric expansion of the hygroscopic sample could be simplified to the height elongation and could be probed by the time of stretching when the detected force turned positive. The samples (15 mg, 9 mm × 30 mm) were fixed at the testing machine and the initial film length between two holders was 20 mm (T = 25 °C, RH = 30%). The RH was controlled by a humidifier and measured by a hygrometer. The data was recorded by textXpert II software. When the RH switched abruptly from 30% to 95%, the film expanded and was stretched at a rate of 4.5 mm·min^{-1} to match the swelling rate. When the RH decreased, the sample steadily shrank to its initial length, and the contractile force was recorded. Three samples were tested, and each test was repeated for five humidifying/drying cycles.

Solvent-Responsive Bending Deformation: The bending deformation of the PPC thin film was monitored by a video camera in a humidity-controlled system, which includes a water container with temperature manipulation through a heating plate underneath, and covered by a nonwoven paper as the moist substrate (composition at the dry state: 60% cellulose and 40% polyester, and saturated with 50 wt.% water during the test). The system is equilibrated in the ambient condition (T = 25 °C, RH = 30%, no detectable air flow) for 20 min to obtain a stable humid environment. The humidity was monitored by a commercial hydro-thermometer. The temperature of the heating plate is kept at 40 °C for stable generation of vapor. The bending angle was used to analyze the bending process. At least three videos were taken and analyzed for each group of samples. The bending speeds were extracted and analyzed by Origin v2022 software. For ethanol and isopropanol, the experiment was carried out in the fume hood with the same setup.

Fabrication of the Athlete Robot: Two athlete robots were fabricated by cutting the PPC thin film into a rectangular shape (width × length: 8 mm × 20 mm, 15 mg). A non-stimuli-responsive cargo (390 mg) was attached to one side of each robot by coating a thin layer of 10 µL super glue (Pattex, Henkel AG, Germany) on the film surface. The athlete robot performed lifting motions when subjected to a humidifying treatment.

Humidity-Responsive Electrical Properties: Electrical impedance spectra were recorded with an IVIUM Vertex 100 mA potentiostat (Ivium Technologies BV, Eindhoven, The Netherlands) at 20 °C and under adjustable humidity. Spectra acquisition was controlled using IviumSoft Software (Version 4.1129) using the measurement settings listed in Table S1 (Supporting Information). The PPC thin film was prepared onto a pre-cleaned glass slide. Two titanium metal blocks were used as electron-conducting but ion-blocking electrodes and were firmly attached on both top ends of the PPC film (60 mm × 15 mm, length × width) using a clamp. Humidity conditions were varied within a custom-built vapor generation system that allowed humidity control of the sample environment. The electrical resistivity of the respective samples while undergoing the varying humidities, was measured in situ by applying a constant current and recording the voltage. The current applied for the chronopotentiometry was 100 mA, and the range of voltage was 1 V.

Tensile Test: The mechanical properties of the PPC thin film were examined by a Zwick Z005 testing machine. Samples with a thickness of 40 ± 5 µm were cut with a size of 40 mm × 8 mm (length × width). The bottom clamp was attached to a 50 N load cell. The stretching rate was 10 mm·min^{-1}. The data was recorded by textXpert II software. Three stripes for each sample were tested at the ambient condition (T = 25 °C, RH = 30%). For simplicity, only one representative strain-stress curve for each sample is shown in the manuscript. The tensile strength and the fracture strain were obtained by averaging the values from three strain-stress curves for each sample.

Microscopic Observation of the Injury: The punctured samples were prepared by stamping a needle through the film, and the stretched samples were obtained by stretching the film at a rate of 10 mm·min^{-1} until failure. The nano and microscopic morphology of the PPC thin film before and after injury was characterized at a high-resolution scanning electron microscope (Gemini SEM 460, Zeiss, Germany) at the Electron Microscopy Center of Empa. The films were coated with a carbon layer (thickness of 10 nm) by the Safematic CCU-010 coating machine before the measurement. SEM micrographs were recorded using the SE2 and in-length electron detector at an accelerating voltage of 2 kV. The healing of the PPC thin film was observed under an optical microscope (ZEISS SteREO Discovery V20) with a 40 × objective.

Ultra-Small-Angle X-Ray Scattering: USAXS experiments were carried out at the P03/MiNaXS beamline at the synchrotron source PETRA III at Deutsches Elektronen Synchrotron (DESY), Hamburg, Germany. The experiments were performed at the energy of 11.8 keV with a wavelength of $\lambda = 0.105$ nm. The beam size was 80 × 56 µm^2 (horizontal × vertical). The sample-detector distance was kept at 9570 ± 5 mm. A Pilatus 2 M detector (Dectris AG, Switzerland) with a pixel size of 172 × 172 µm^2 was used for USAXS. A defined humidity control protocol was used for the in situ USAXS measurement. A total flow of 1000 mL·min^{-1} of mixed dry and wet nitrogen was introduced into the cell, which was sealed with a Kapton window to allow for sufficient X-ray beam transmission. The humidifying/drying cycle contains 21 steps, which include the RH increase from 0% to 100% and decrease from 100% to 0%, with each step being 10% of RH.

Statistical Analysis—FTIR: PPC samples for FTIR were cut into a square shape (5 mm × 5 mm, length × width). The data was recorded by OPUS v8.9 software and analyzed by Origin v2022 software. Three series of FTIR spectra were recorded for each of the three samples within one D_2O soaking/H_2O exchange cycle, and the spectra of one representative sample were selected for analysis.

Statistical Analysis—DVS: Three PPC thin films (arbitrary shape, 10 mg) were used for DVS analysis. The data was recorded by TRIOS v5.1.1 software and averaged by Origin v2022 software.

Statistical Analysis—DMA: Three PPC thin films (60 mm × 8 mm, length × width) were prepared and measured under three representative RH levels, respectively. The equilibrium data point at the desired RH level was recorded by Orchestrator v7.2.0.4 software and averaged by Origin v2022 software.

Statistical Analysis—Quantification of the Bending Deformation: PPC thin films with a sample size of 15 mm × 5 mm (length × width) were used to monitor the humidity-responsive bending deformation. One side of the rectangular sample was fixed onto a non-humidity-responsive sample holder, and the movement of the other unbounded side of the sample was recorded by a video camera. The position of the unbounded side was extracted at every 0.1 s. The bending angle was calculated according to Figure S6 (Supporting Information). At least three videos were taken and analyzed for each sample. The variation of the bending angle with respect to time was analyzed by Origin v2022 software.

Statistical Analysis—Tensile stretching: Step 1) To quantify the internal stress induced by water absorption/desorption, the PPC sample with a size of 9 mm × 30 mm (length × width) was fixed at the testing machine with

the initial film length between the holders being 20 mm. When the RH was abruptly increased, a stretching rate of 4.5 mm min^{-1} was applied. Three samples were tested, and the results from one representative sample were selected for analysis. 2) To characterize the mechanical properties before and after injury, the PPC sample with a size of 40 mm × 8 mm (length × width) was used for testing. For each testing condition, three samples were prepared and tested to obtain the average value of tensile strength, and elongation-at-break, and only one representative strain-stress curve was selected as the representative data. The data was recorded by textXpert II software and analyzed by Origin v2022 software.

Statistical Analysis—Impedance Measurement: Three drop-casted PPC thin films were directly used for impedance measurement. The size of each sample is 60 mm × 15 mm (length × width). The impedance spectra of three PPC thin films were tested stepwise during the humidifying cycle, and the spectra of one representative sample were used for analysis in the manuscript. Spectra acquisition was controlled using IviumSoft v4.1129 software. The data was analyzed by Origin v2022 software.

Statistical Analysis—USAXS: The size of PPC thin films for USAXS measurements was kept at 10 mm in length and 2 mm in width. To obtain a quantitative analysis of the structural information, azimuthal cuts of the USAXS data were made by DPDAK v 1.5.0 software in the indicated region from $q = 0.037$ nm^{-1} to $q = 0.71$ nm^{-1}. The calculation of the SLD of PEDOT:PSS and NaCMC was conducted by the "Scattering Length Density Calculator" from the website https://www.ncnr.nist.gov/. The calculated SLD of PEDOT:PSS and NaCMC was 9×10^{-6}·$Å^{-2}$ and 14×10^{-6}·$Å^{-2}$, respectively. All modeling of the USAXS curves was done using SASView v5.0.3 software, which is an open-source analysis software for small-angle scattering data. Three structural models were used for the fitting of the data. The sphere model provided spheres with uniform scattering length density. The cylinder model provided a circular cylinder with uniform scattering length density. The flexible cylinder model included a chain of some number of locally stiff segments. The average structural parameters of these models were extracted from SEM images by ImageJ v1.8.0 software to restrict the flexibility of the fits. After fitting, the χ^2 -values were used as an indicator for evaluation of the most suitable fits.

Statistical Analysis—Calculation of Healing Efficiency: The healing efficiency (η) of the PPC thin film was calculated in terms of the restoration of the toughness (Equation 1),

$$\eta = \frac{U_{\text{T-healed}}}{U_{\text{T-pristine}}} \times 100\% \quad (1)$$

where $U_{\text{T-healed}}$ and $U_{\text{T-pristine}}$ represent the toughness of the non-injured and healed samples, respectively. The healing efficiency was also calculated in terms of the humidity-responsive bending speed (Equation 2),

$$\eta = \frac{\kappa_{\text{healed}}}{\kappa_{\text{pristine}}} \times 100\% \quad (2)$$

where κ_{healed} and κ_{pristine} represent the bending speed of the healed sample and its pristine counterpart.

Supporting Information

Supporting Information is available from the Wiley Online Library or from the author.

Acknowledgements

This research was funded by the European Union's Horizon 2020 research and innovation program under grant agreement No. 964388 as COgITOR: A new COlloidal cybernetIc sysTem tOwaRd 2030. P.M.-B. acknowledges funding from the German Ministry for Education and Research (BMBF) project "Flexiprob" (grant no. 05 K2016). The authors acknowledge Prof. Frank Nüesch (Empa Laboratory of Functional Polymers) for giving access to the FTIR measurement, and Dr. Robin Pauer for his support in the SEM experiments. The authors acknowledge DESY (Hamburg, Germany), a member of the Helmholtz Association HGF, for the provision of experimental facilities. Part of this research was carried out at the P03 beamline. The authors are thanking Matteo Bevione (Empa) for assistance with data acquisition. Beamtime was allocated for the proposal I-20220029. This work benefited from the use of the SasView application, originally developed under NSF award DMR-0520547. SasView contains code developed with funding from the European Union's Horizon 2020 research and innovation program under the SINE2020 project, grant agreement No 654000.

Open access funding provided by ETH-Bereich Forschungsanstalten.

Conflict of Interest

The authors declare no conflict of interest.

Data Availability Statement

The data that support the findings of this study are available from the corresponding author upon reasonable request.

Keywords

actuator, healing, humidity-responsive, structural rearrangement

Received: February 19, 2024
Revised: May 6, 2024
Published online: May 23, 2024

[1] X. Q. Wang, G. W. Ho, *Mater. Today* **2022**, *53*, 197.
[2] M. Li, A. Pal, A. Aghakhani, A. Pena-Francesch, M. Sitti, *Nat. Rev. Mater.* **2022**, *7*, 235.
[3] S. Zhang, X. X. Ke, Q. Jiang, Z. P. Chai, Z. G. Wu, H. Ding, *Adv. Mater.* **2022**, *34*, 2200671.
[4] D. Cho, J. S. Jang, S. H. Nam, K. Ko, W. Hwang, J. W. Jung, J. Lee, M. Choi, J. W. Hong, I. D. Kim, S. Jeon, *ACS Nano* **2020**, *14*, 12173.
[5] J. M. McCracken, B. R. Donovan, T. J. White, *Adv. Mater.* **2020**, *32*, 1906564.
[6] X. Q. Wang, K. H. Chan, Y. Cheng, T. P. Ding, T. T. Li, S. Achavananthadith, S. Ahmet, J. S. Ho, G. W. Ho, *Adv. Mater.* **2020**, *32*, 2000351.
[7] H. L. Li, M. Kruteva, K. Mystek, M. Dulle, W. H. Ji, T. Pettersson, L. Wågberg, *ACS Nano* **2020**, *14*, 6774.
[8] L. A. E. Müller, A. Zingg, A. Arcifa, T. Zimmermann, G. Nyström, I. Burgert, G. Siqueira, *ACS Nano* **2022**, *16*, 18210.
[9] S. Terryn, J. Langenbach, E. Roels, J. Brancart, C. Bakkali-Hassani, Q. A. Poutrel, A. Georgopoulou, T. G. Thuruthel, A. Safaei, P. Ferrentino, T. Sebastian, S. Norvez, F. Iida, A. W. Bosman, F. Tournilhac, F. Clemens, G. Van Assche, B. Vanderborght, *Mater. Today* **2021**, *47*, 187.
[10] Y. Zhao, M. Hua, Y. Yan, S. Wu, Y. Alsaid, X. He, *Annu. Rev. Control Robot. Auton. Syst.* **2022**, *5*, 515.
[11] M. Khatib, O. Zohar, H. Haick, *Adv. Mater.* **2021**, *33*, 2004190.
[12] S. V. Wanasinghe, O. J. Dodo, D. Konkolewicz, *Angew Chem. Int. Ed. Engl.* **2022**, *61*, 202206938.
[13] N. Zheng, Y. Xu, Q. Zhao, T. Xie, *Chem. Rev.* **2021**, *121*, 1716.
[14] Y. Wang, X. Huang, X. Zhang, *Nat. Commun.* **2021**, *12*, 1291.
[15] Y. Wang, G. Su, J. Li, Q. Guo, Y. Miao, X. Zhang, *Nano Lett.* **2022**, *22*, 5409.
[16] X. Z. Lin, F. Li, Y. Bing, T. Fei, S. Liu, H. R. Zhao, T. Zhang, *Nano-Micro Lett.* **2021**, *13*, 200.

[17] W. B. Ying, G. Wang, Z. Kong, C. K. Yao, Y. Wang, H. Hu, F. Li, C. Chen, Y. Tian, J. Zhang, R. Zhang, J. Zhu, *Adv. Funct. Mater.* **2021**, *31*, 2009869.
[18] J. W. Kim, H. Park, G. Lee, Y. R. Jeong, S. Y. Hong, K. Keum, J. Yoon, M. S. Kim, J. S. Ha, *Adv. Funct. Mater.* **2019**, *29*, 1905968.
[19] H. L. Qin, T. Zhang, N. Li, H. P. Cong, S. H. Yu, *Nat. Commun.* **2019**, *10*, 2202.
[20] H. Q. Tao, D. W. Yue, C. H. Li, *Macromol. Mater. Eng.* **2022**, *307*, 2100649.
[21] X. B. Zhu, W. J. Zhang, G. M. Lu, H. C. Zhao, L. P. Wang, *ACS Nano* **2022**, *16*, 16724.
[22] C. J. Brett, O. K. Forslund, E. Nocerino, L. P. Kreuzer, T. Widmann, L. Porcar, N. L. Yamada, N. Matsubara, M. Månsson, P. Müller-Buschbaum, L. D. Söderberg, S. V. Roth, *Adv. Electron. Mater.* **2021**, *7*, 2100137.
[23] V. T. Tran, M. T. I. Mredha, Y. Lee, M. Todo, H. So, E. Jeong, W. Park, I. Jeon, *Adv. Funct. Mater.* **2022**, *32*, 2100177.
[24] J. Tolvanen, M. Nelo, H. Alasmaki, T. Siponkoski, P. Makela, T. Vahera, J. Hannu, J. Juuti, H. Jantunen, *Adv. Sci.* **2022**, *9*, 2205485.
[25] S. Zhang, F. Cicoira, *Adv. Mater.* **2017**, *29*, 1703098.
[26] W. Chen, Y. H. Bu, D. L. Li, C. J. Liu, G. X. Chen, X. F. Wan, N. Li, *Cellulose* **2020**, *27*, 853.
[27] W. Li, B. Sun, P. Wu, *Carbohydr. Polym.* **2009**, *78*, 454.
[28] B. C. Wang, J. G. Torres-Rendon, J. C. Yu, Y. M. Zhang, A. Walther, *ACS Appl. Mater. Interfaces* **2015**, *7*, 4595.
[29] D. Zhao, Y. Zhu, W. Cheng, G. Xu, Q. Wang, S. Liu, J. Li, C. Chen, H. Yu, L. Hu, *Matter* **2020**, *2*, 390.
[30] M. M. Ma, L. Guo, D. G. Anderson, R. Langer, *Science* **2013**, *339*, 186.
[31] S. K. Reinke, S. V. Roth, G. Santoro, J. Vieira, S. Heinrich, S. Palzer, *ACS Appl. Mater. Interfaces* **2015**, *7*, 9929.
[32] M. Ganesan, R. Kumar, D. K. Satapathy, *Langmuir* **2022**, *38*, 6066.
[33] M. Wieland, C. Dingler, R. Merkle, J. Maier, S. Ludwigs, *ACS Appl. Mater. Interfaces* **2020**, *12*, 6742.
[34] A. L. Oechsle, T. Schoner, L. Deville, T. Xiao, T. Tian, A. Vagias, S. Bernstorff, P. Müller-Buschbaum, *ACS Appl. Mater. Interfaces* **2023**, *15*, 47682.
[35] Y. Lu, Y. F. Men, *Macromol. Mater. Eng.* **2018**, *303*, 1800203.
[36] A. Buffet, A. Rothkirch, R. Dohrmann, V. Korstgens, M. M. A. Kashem, J. Perlich, G. Herzog, M. Schwartzkopf, R. Gehrke, P. Muller-Buschbaum, S. V. Roth, *J. Synchrotron Radiat.* **2012**, *19*, 647.
[37] E. A. Chernova, D. I. Petukhov, A. P. Chumakov, A. V. Kirianova, I. S. Sadilov, O. O. Kapitanova, O. V. Boytsova, R. G. Valeev, S. V. Roth, A. A. Eliseev, A. A. Eliseev, *Carbon* **2021**, *183*, 404.
[38] A. A. Eliseev, A. A. Poyarkov, E. A. Chernova, A. A. Eliseev, A. P. Chumakov, O. V. Konovalov, D. I. Petukhov, *2D Mater.* **2019**, *6*, 035039.
[39] Q. Chen, B. Sochor, A. Chumakov, M. Betker, N. M. Ulrich, M. E. Toimil-Molares, K. Gordeyeva, L. D. Söderberg, S. V. Roth, *Adv. Funct. Mater.* **2022**, *32*, 2208074.
[40] D. Belaineh, J. W. Andreasen, J. Palisaitis, A. Malti, K. Håkansson, L. Wågberg, X. Crispin, I. Engquist, M. Berggren, A. C. S. Appl, *Polym. Mater.* **2019**, *1*, 2342.
[41] M. Doucet, J. H. Cho, G. Alina, Z. Attala, J. Bakker, W. Bouwman, P. Butler, K. Campbell, T. Cooper-Benun, C. Durniak, L. Forster, M. Gonzales, R. Heenan, A. Jackson, S. King, P. Kienzle, J. Krzywon, T. Nielsen, L. O'Driscoll, W. Potrzebowski, S. Prescott, R. F. Leal, P. Rozycko, T. Snow, A. Washington, SasView version 5.0.3, https://zenodo.org/record/3930098 (accessed: May 2024).
[42] H. Zhang, L. Cao, J. Li, Y. Liu, Z. Lv, J. Ren, Z. Shao, S. Ling, *Chem. Mater.* **2023**, *35*, 1752.